Soil cation storage is a key control on the carbon removal dynamics of enhanced weathering

Authors: Y. Kanzaki[1*], N.J. Planavsky[2,3], S. Zhang[4], J. Jordan[5], [3,2]T.J. Suhrhoff, C.T. Reinhard[1*]

Affiliations:

[1]School of Earth and Atmospheric Sciences, Georgia Institute of Technology, Atlanta, GA, USA.
[2]Department of Earth and Planetary Sciences, Yale University, New Haven, CT, USA.
[3]Yale Center for Natural Carbon Capture, New Haven, CT, USA.
[4]Department of Oceanography, Texas A&M University, College Station, TX, USA.
[5]Porecast Research, LLC, Lawrence, KS, USA.

[*]corresponding author: ykanzaki3@gatech.edu, chris.reinhard@eas.gatech.edu

Key Points:

- Cation storage in soils can temporarily undo the carbon dioxide removal that occurs during the enhanced weathering process.
- Lags in carbon removal after carbonate or silicate weathering can vary from years to many decades.
- Carbon removal lags should be quantified in enhanced weathering deployments through rigorous validation of models with real-world data.

Plain Language Summary: Adding rock powder to agricultural lands - a process called enhanced weathering - can potentially remove carbon dioxide from Earth's atmosphere and help to mitigate the impacts of climate change. However, agricultural soils can also store the products of enhanced weathering, which could delay carbon removal for years or even decades. Climate mitigation strategies that involve enhanced weathering must incorporate this lag effect in order to be robust.

Abstract: Significant interest and resources are currently being channeled into techniques for durable carbon dioxide removal (CDR) from Earth's atmosphere. A particular class of these approaches — referred to as enhanced weathering — seeks to modify the surface alkalinity budget to store CO_2 as dissolved inorganic carbon species. Here, we use a reaction-transport model designed to simulate enhanced weathering in managed lands to evaluate the throughput and storage timescales of anthropogenic alkalinity in agricultural soils in the coterminous U.S. We find that lag times between alkalinity modification and carbon removal can span from years to many decades depending on region. Background soil cation exchange capacity, agronomic target pH, and fluid infiltration all impact the timescales of CDR relative to the timing of alkalinity input, suggesting there is scope for optimization of alkalinity transport through variation in land management practice. However, shifting practices to reduce lag times may decrease total CDR from weathering and lead to non-optimal nutrient use efficiencies and soil nitrous oxide (N_2O) fluxes. Our results indicate that there may be a large temporal disconnect between deployment of enhanced weathering and climate-relevant CDR, with important implications for monitoring, reporting, and verifying carbon removal through enhanced weathering.

1. Introduction

Efforts to limit the extent of future anthropogenic climate disruption will likely require significant amounts of net carbon dioxide removal (CDR) from Earth's atmosphere. Even optimistic scenarios for decarbonization of energy systems, transport, and industry in the coming decades still require roughly 1-10 gigatons (Gt = 10^9 tons) of carbon dioxide to be removed from the atmosphere each year by the end of the century to achieve net carbon neutrality [1, 2]. The current supply of durable CDR — defined as carbon removal that is durable on timescales similar to or greater than the residence time of CO_2 in the atmosphere (~10^2 years) — is many orders of magnitude below this [3]. There is thus strong impetus for developing promising durable CDR approaches, and significant amounts of private and public funding flowing into efforts to develop the basic science underlying durable CDR pathways and bring them to scale.

Enhanced weathering (EW) is one promising geochemical approach toward durable CDR [4-10]. This practice involves adding fine-grained cation-rich rock feedstocks (basalt, olivine, wollastonite, or steel slag) to soils, where they dissolve in the presence of elevated soil CO_2 to yield bicarbonate (HCO_3^-). This bicarbonate can be transported by river/stream systems to the oceans, where much of it will remain stored on timescales on the order of 10^4 years [9, 11, 12]. Carbonate (limestone) weathering – currently in widespread use as an agricultural practice for soil pH management – can also lead to alkalinity export and CDR. However, the dynamics of this process are dependent in part on the pH at which weathering occurs, because bicarbonate produced from weathering reactions is unstable at relatively low soil pH [13, 14]. In any case, because EW has the potential to leverage extensive existing agricultural infrastructure, requires relatively little energy beyond that required to transport feedstock, and may have a range of agronomic and socioeconomic co-benefits, it has attracted considerable interest as a durable, cost-effective CDR pathway that has the potential to scale rapidly [5, 10, 15, 16].

However, there is a range of possible fates for cations released from EW feedstocks, including calcium carbonate or secondary clay mineral formation in terrestrial settings [17, 18], re-equilibration of the carbonic acid system in rivers and streams [8, 19, 20], and storage of cations on exchange sites within soils and in the lower critical zone [21-23]. In the case of secondary mineral formation, CO_2 can be permanently released back to the atmosphere, undoing the initial CDR. In the case of cation storage on exchange sites within soils CDR is instead delayed. In most instances cation sorption will drive conversion of HCO_3^- to CO_2 due to release of exchangeable acidity from the soil (**Fig. 1**), which is then rebalanced by HCO_3^- production once reversibly sorbed cations are released from the soil exchange complex when soils re-acidify.

Methods are currently being developed for tracking the initial release of cations from EW feedstocks [e.g., 24, 25, 26], and these approaches can provide an estimate of the "potential CDR" at the initial point of feedstock dissolution. However, the timescales over which this CDR potential will be realized are poorly known [16, 27]. This is critical for the technoeconomics of EW, because a ton of carbon removed immediately has more value than a ton of carbon removed in the future [e.g., 28, 29-31]. As a result, offset purchase contracts using EW as a pathway should either accurately discount lagged carbon removal *ex-ante* or have *ex-post* guardrails for empirically verifying cation fluxes through the system over time. In either case, timescales of cation lag that are sufficiently long could potentially render project finance for EW deployments less favorable for conventional voluntary carbon markets.

Here, we use a reaction-transport code [32, 33] designed to simulate enhanced weathering (EW) in managed lands to evaluate the throughput and storage timescales of anthropogenic alkalinity in agricultural soils. Through a series of idealized alkalinity flux simulations, we explore the main controls on cation storage and export from surface soils in key U.S. agricultural regions. We find that carbon removal lags induced by transient cation storage in soils can range from years to many decades — varying significantly across key agricultural regions of the U.S. — and suggest that carbon removal lags due to cation storage need to be considered in future EW research and deployment efforts. Lastly, we discuss the implications of these results for implementation of EW within carbon markets and suggest potential strategies through which background soil characteristics and deployment practice can both be leveraged to shorten carbon removal lags.

2. Materials and Methods

2.1 A gridded dataset for simulated alkalinity modification in U.S. agricultural regions

We focus here on key agricultural regions of the coterminous United States, basing our analysis on areas with a cropland fraction greater than 10% and gridded at a resolution of 1°x1°. As boundary conditions for the initialization and spin-up of our reaction-transport code we use a series of gridded data products for runoff (defined as the sum of quick-flow runoff, recharge, and irrigation as in [34]), mean annual air temperature (MAT), soil moisture, aboveground net primary productivity (NPP), soil organic matter (SOM), fertilization rate, topsoil pH, soil cation exchange capacity (CEC), and soil base saturation (**Fig. 2**). All observational data are from the sources shown in **Table** 1, and are either derived from the uppermost soil layer (0 to 20 or 30 cm, depending on the database) or averaged over the top 30 cm when depth-resolved at higher resolution. Data products are at a native resolution of 1°x1° or higher, with high-resolution data area-weighted and re-gridded to 1°x1°. The partial pressure of CO_2 in the soil (pCO_2) was calculated as a function of net primary production (NPP) and temperature according to the method of Gwiazda and Broecker [35], as adapted and modified by Goddéris et al. [36], Gaillardet et al. [37], and Zeng et al. [38].

The reaction-transport model used here is designed to track feedstock-specific alkalinity release and cation/carbon biogeochemistry in managed soils [32, 33]. We adopt a model configuration that is essentially the same as that described in [32], which consists of two solid species (bulk soil phase plus soil organic matter), one gaseous species (CO_2), and an inclusive range of aqueous species for evaluating charge balance and soil acid-base balance [33]. We use four tuning parameters to initialize the soil column in each grid cell: (1) an aggregate cation exchange parameter ($K_{H/Na}$), which is then used to scale exchange parameters for all other cations; (2) a dissolved Ca^{2+} concentration at the upper boundary of the soil column, which essentially represents background carbonate weathering and historical agricultural liming; (3) an input flux of organic carbon (OC) to the soil; and (4) a time constant for organic carbon turnover (**Fig. 3**). These parameters are tuned to match the observed values for soil pH, base saturation, soil organic matter content, and estimated soil pCO_2 (**Fig. 2**), with the soil column in each grid cell being spun up for 10^5 years prior to alkalinity modification. Comparison of our baseline tuned parameter set (**Fig. 3**) with a range of observational data is provided in the **Supporting Information**.

Following spinup and initialization, we conduct alkalinity modification experiments in which an alkaline feedstock is added at a rate is iteratively tuned to reach a specified agronomic target pH ($pH_t = 7.0$) at the end of each year for 100 years. We implement two alkalinity sources — a default CaO feedstock, which is characterized by extremely rapid dissolution kinetics and simple cation stoichiometry, and an "instantaneous" basalt feedstock, which has the stoichiometry of the idealized glassy basalt used by [32] but is specified to dissolve with the same speed as the CaO feedstock. This approach is designed to remove the time-dependent uncertainty in feedstock dissolution rates and to isolate the effects of cation exchange on the timescales of CDR. In the simulations shown here, feedstock is added continuously for each year and mixed homogeneously down to a depth of 25cm. In-silico agronomic soil pH is calculated by the method described in [32]. The model domain for all simulations is 50 cm, which for our purposes is expected to yield a conservative (i.e., lower-bound) estimate of cation travel times through the soil column given that in the field cations will generally need to travel longer distances before being exported.

The boundary conditions of the reactive transport model are described in [33] and [32]. Briefly, the lower boundary is a parent rock composition for the solid phase and a zero-flux boundary for aqueous and gaseous phases. The upper boundary is a fixed composition for aqueous and gaseous species. The model allows for transport of solid, aqueous, and gaseous phases through advection and mixing, advection and diffusion/dispersion, and diffusion, respectively. Here, advection of solids and fluids is constrained respectively from USDA soil erosion rate data and runoff [34], while soil moisture impacts gaseous phase transport by modifying the soil tortuosity and diffusivity. The reaction kinetics are simulated for heterogeneous decomposition/formation of solid phases and redox reactions [33] and equilibrium is assumed for aqueous speciation and cation exchange [32, 33]. We also conduct control experiments branched from the same initialization/spinup as that of the alkalinity modification experiments with identical boundary conditions other than the addition of alkaline feedstock.

2.2 CDR calculation methods

We evaluate CDR over time in the simulated soil column using three metrics, each of which is designed to correspond to a distinct set of techniques for measurement, reporting, and verification (MRV) of CDR in enhanced weathering deployments. The first is scaled to the fraction of feedstock that dissolves in the soil (CDR_{diss}):

$$CDR_{diss} = \frac{\sum_\theta \gamma_\theta \Delta J_\theta^{diss}}{\sum_\theta \gamma_\theta \Delta J_\theta^{feed}} \quad , \tag{1}$$

where γ_θ is the molar ratio of potential CO_2 capture per unit dissolution of feedstock θ (e.g., $\gamma_{CaO} = 2$), J_θ^{feed} and J_θ^{diss} are deployment (spreading) and dissolution fluxes of feedstock θ (mol m^{-2} y^{-1}), respectively, and Δ denotes the flux difference between scenarios with and without feedstock deployment. Mechanistically, this metric corresponds to time-integrated solid-phase approaches for tracking on-field rates of CDR [4, 24, 25, 39, 40], which rely on measuring mobile cations and immobile elements in soil before and after feedstock application and using these measurements to estimate loss of base cations from applied feedstock.

The second CDR metric employed here is scaled to the reduction of gaseous CO_2 exchange between the soil column and the atmosphere (CDR_{diff}):

$$CDR_{diff} = \frac{\Delta J_{CO_2} - \Delta J_{SOC}}{\sum_\theta \gamma_\theta \Delta J_\theta^{feed}} \quad , \tag{2}$$

where γ_θ, J_θ^{feed}, and Δ are defined as above and J_{CO_2} and J_{SOC} are the soil-atmosphere flux of CO_2 (mol m^{-2} y^{-1}) and the decomposition flux (mol m^{-2} y^{-1}) of soil organic carbon (SOC), respectively.

Mechanistically, this metric reflects a decrease in the flux of CO_2 from the soil column to the atmosphere due to HCO_3^- production in the soil, and could in principle be measured through CO_2 gas fluxes from treated and control soils via eddy flux towers [41], flux chambers [42], or gas-phase CO_2 sensors [43]. In contrast to the solid-phase metric shown by Eq. (1), this metric tracks CDR directly and reflects additional HCO_3^- production (and a corresponding reduction of the soil-atmosphere CO_2 flux) due to soil management.

Lastly, we can scale CDR efficiency to the increase in advective fluxes of aqueous dissolved inorganic carbon species through the soil column (CDR_{adv}):

$$CDR_{adv} = \frac{\Delta J_{DIC} - \Delta J_{SIC}}{\sum_\theta \gamma_\theta \Delta J_\theta^{feed}} \quad , \tag{3}$$

where γ_θ, J_θ^{feed}, and Δ are defined as above and J_{SIC} and J_{DIC} represent the flux (mol m^{-2} y^{-1}) of soil inorganic carbon (i.e., mineral carbonates) dissolving into the soil system and total dissolved inorganic carbon (i.e., aqueous CO_2, HCO_3^-, and CO_3^{2-}) advected out of soil column, respectively. Mechanistically, this metric reflects additional HCO_3^- production and advection out of the system due to feedstock application and could in principle be determined by an aqueous measurement at the field scale (e.g., alkalinity fluxes using a lysimeter [44]), point-collected dissolved solute measurements at the catchment scale [45] , or possibly at larger scales through measurements of solute composition in stream/river systems [e.g., 13]. Similar to Eq. (2), this metric directly tracks net CDR in the soil column rather than gross alkalinity release.

Note that these metrics for CDR efficiency are referenced to the maximum potential CDR (e.g., $\sum_\theta \gamma_\theta \Delta J_\theta^{feed}$), which assumes that all base cations released from feedstock θ are leached immediately upon deployment and charge-balanced only by production of bicarbonate ions. At steady state, the reduction in soil-atmosphere CO_2 flux should be equivalent to the increase in bicarbonate advection ($CDR_{diff} \sim CDR_{adv}$). In the case of negligible cation sinks (e.g., secondary carbonate or silicate mineral phases) and on arbitrarily long timescales, $CDR_{diss} \sim CDR_{diff} \sim CDR_{adv}$. However, transient cation storage could result in lag periods for which CDR_{diff} (or CDR_{adv}) $<$ CDR_{diss}. This allows us to isolate and quantify cation storage lags through time-dependent offsets between CDR_{diss} and CDR_{diff}/CDR_{adv}.

3. Results

We first examine timescales of alkalinity release, cation exchange, and carbon removal in four representative sites across key agricultural regions in the U.S.: (1) Site 128, located in the Northern Plains region; (2) Site 311, located in the Corn Belt; (3) Site 161, located in the Southern Plains region; and (4) Site 411, located in the Southeast (**Fig. 2, 3**). Alkalinity release into the system is specified to be effectively instantaneous across all sites (**Fig. 4**), with dissolution-based CDR (CDR_{diss}) matching effective CDR potential (CDR_{eff}) on a timescale of days to weeks. However, most of the alkalinity released from feedstock is initially stored as exchangeable calcium (Ca_{exch}) and is only gradually released back into the system as an advective cation flux (Ca_{adv}) over timescales ranging from years to decades (**Fig. 4**). This causes a significant lag in carbon removal relative to alkalinity input because it is only when the exchangeable calcium is released into the advective flux and charge balanced by HCO_3^- production that CDR can occur.

Although there is often a slight offset between carbon removal based on soil-atmosphere CO_2 exchange (CDR_{diff}) and advection of new DIC (CDR_{adv}) in the first decade, they track each other closely. However, actual carbon removal (tracked by both CDR_{diff} and CDR_{adv}) occurs over significantly longer timescales than those of alkalinity release (tracked by CDR_{diss}, here set to be effectively instantanous) across all sites (**Fig. 4**). For example, for our deployment in the Corn Belt CDR_{diff} and CDR_{adv} reach less than 50% of the effective CDR potential after 10 years, with a timescale of over 50 years required to reach 80% of effective carbon removal (**Fig. 4b**). In contrast, realized CDR reaches nearly 80% of its potential within the first decade after deployment in the Southeast regional site (**Fig. 4d**).

Because the timescale required to achieve a particular CDR potential varies by region, we geospatially aggregate and weight carbon removal lags by overall alkalinity flux across key agricultural regions in the U.S. (**Fig. 5**). There are relatively few sites that show any tangible carbon removal in the first year despite instantaneous cation and alkalinity inputs, and these are generally restricted to scattered locations in the southeastern U.S. (Alabama, Georgia, and Florida; **Fig. 5a,e**). Many of the regions examined here show widespread areas that are below 50% of effective CDR potential after 5 years, and in some regions (the Corn Belt and Great Plains) it takes well over 10 years after instantaneous alkalinity input for carbon removal to occur locally (**Fig. 5d,h**). We find that instantaneous basalt simulations result in greater CDR at any given time, locally approaching nearly 10% of additional CDR capacity relative to the feedstock potential (**Fig. 5i-l**). This is due to the more complex cation stoichiometry of basalt, which in addition to Ca^{2+} contains a small amount of Na^{+} that flushes through the system rapidly. This effect is most significant within the first ~5 years of simulated deployment (**Fig. 5j**), but we would expect the magnitude and time dynamics of this effect to vary as a function of major cation chemistry of silicate feedstocks.

Although local CDR lags induced by cation storage can be high, in many cases regionally aggregated and flux-weighted CDR lags are much shorter. For instance, for key agricultural regions in the Midwest, Southeast, and Pacific regions flux-weighted CDR lags on achieving 50% CDR capacity are roughly 10, 3, and 7 years, respectively (**Fig. 6**). For CONUS croplands as a whole the flux-weighted lag times to achieve 25%, 50%, and 75% of CDR capacity are, respectively, 5, 8, and 22 years (**Fig. 6**). Lags on CDR induced by soil cation storage are thus expected to vary by orders of magnitude across scales, both at the field scale and when regionally aggregated, but in general our analysis suggests that over 50% of CDR capacity should be achievable within a decade of alkalinity release across all of the regions analyzed here.

The magnitude of cation lag should vary as a function of background soil characteristics. This is evident, for example, in the Southeast sites which, on average, show significantly shorter lag times overall because of very low cation exchange capacities and high water fluxes (**Fig. 2h, 5a,e, 6b**). Cation lag times should also be impacted by soil management practice — particularly the soil pH targeted for a given crop rotation or soil tilling style. For example, we find that higher target pH values can result in significantly higher CDR efficiency across the first few decades of increasing soil base saturation (**Fig. 7**) because of more rapid cation loading on the soil exchange complex. The impact of this can be significant – at Site 411, for instance, a target pH value of 5.5 results in an advective CDR efficiency of ~30% after ten years, while the same CDR efficiency can be achieved in only ~3 years at a target soil pH value of 7 (**Fig. 7**). The aggregate impacts of this will depend on the intersection between EW deployment strategy and agronomic practice, as target pH will depend on cash crop — many staple crops in the U.S. do well at soil pH values up to ~7, while some forage and specialty crops prefer more acidic pH [46].

4. Discussion

Our results suggest that carbon dioxide removal lags induced by cation exchange in agricultural soils can be significant, and in some cases can last multiple decades, adding to a robust evidence base for the following key conclusions: (1) cation sorption in soils with low base saturation (the ratio of cations to protons and aluminum in soil sorption sites) will delay climate-relevant CO_2 removal in EW deployments; (2) this lag time can be multiple years or even several decades locally; and (3) these lag times will vary geographically as a result of soil composition and climatology. Although we stress that although these basic conclusions are very likely robust, we do not currently have firm constraints on the uncertainty in lag times for any individual region or deployment protocol, and there is a pressing need to validate model estimates of carbon removal lag against real-world observations. As a result, we suggest that given the current state of knowledge reaction-transport models are not equipped to provide robust estimates of CDR lag for ready inclusion in carbon accounting schemes [e.g., 47].

One implication of the results presented here is that solid-phase tracers of cation release from EW feedstocks do not represent actual CDR at any time point, but rather a "potential" CDR that may or may not be realized over a wide range of time horizons. Specifically, the condition that $CDR_{diss} >> CDR_{adv}$ is ubiquitous spatially and persists for extended periods of time throughout the regions explored by our model ensemble. This supports a view articulated in previous attempts to use soil-based tracers of cation flux in the field that these tracers are tracking an idealized CDR potential rather than carbon removal itself [4, 24, 25]. Even if the idealized carbon removal potential of a particular feedstock is ultimately realized over a relatively short timescale, we argue that it is important to be as precise as possible when discussing the parameters that a given approach toward field-based MRV is tracking. This is particularly true for for-profit actors making compensatory claims on fossil fuel emissions.

There may be scope for optimizing the efficiency of alkalinity transport through soils via both deployment siting and land management practice. For instance, continuously managing soil pH at a uniform optimal agronomic value is unlikely to be pursued in practice. Instead, pulsed alkalinity addition followed by cation flushing with strong acid from fertilizer application may increase the efficiency of alkalinity transport in managed soils. On the other hand, this approach may lead to lower time-integrated CDR overall. In addition, soil pH is a key driver of soil N_2O emissions through both direct impacts on microbial metabolism and ecosystem structure [48, 49] and through changes to crop nutrient use efficiency [NUE; 50, 51, 52]. As a result, intentional cation flushing could potentially increase time-integrated N_2O emissions, as this practice would be expected to result in extended periods of non-optimal soil pH for crop uptake and more acidic soil pH values overall, both of which could enhance soil N_2O emissions. Optimizing agricultural systems for overall mitigation of CO_2-equivalent emissions (considering both CO_2 removal and N_2O emissions reduction) is an important topic for future work.

From a project siting perspective, regions with relatively low CEC values, large fluid infiltration rates, and increased pH and base cation abundance in the exchange complex at depth [e.g., 53] should all favor more rapid alkalinity export. Our simulations suggest that these conditions are particularly widespread in the Southeastern U.S. However, the tradeoffs between local/regional soil characteristics, optimal agronomic pH for a given local crop rotation, and the counteracting impacts of soil pH on the effectiveness of alkalinity export and initial feedstock dissolution are likely to be complex in practice. In addition, our simulation design intentionally neglects transient or permanent removal of base cations in deeper soils or during transport to the ocean in order to isolate the impacts of the soil exchange complex. Moving forward, there is significant scope for end-to-end analysis of base cation transport efficiency including these additional impacts, and a pressing need for systematic model intercomparison and data-model validation.

An extended carbon removal lag after weathering induced by soil cation exchange has several significant implications for deployment of EW in a market framework. Most importantly, the economic value of carbon removal is time-varying, which means that EW deployments that aim to sell carbon offsets on a voluntary market should be able to accurately quantify the timing of climate-relevant CDR across timescales. One reasonable conclusion might be that suppliers of EW-based offsets on a voluntary market should be expected to either confront the technical challenge of quantifying carbon removal lags prior to deployment or the challenges to project finance associated with empirically verifying carbon removal over extended timescales prior to receiving revenue for offset production. Regardless, our results suggest that cation storage is ubiquitous, highly variable, and should be considered in EW deployments.

Perhaps most importantly, our results highlight the need for more empirical constraints on cation and alkalinity throughput in managed lands across scales. Accurate representation of the soil exchange complex in process-based models such as that explored here is challenging, and there is currently significant uncertainty in the dynamics of cation breakthrough in managed soils that are well out of steady state. Moving forward, the production of large datasets that can constrain cation fluxes and carbon removal lag times, some of which could be produced by private-sector suppliers of carbon removal through EW, would represent a major step forward in our ability to accurately quantify cation storage across a range of scenarios and deployment strategies. There is a pressing need for these data to be rigorously and transparently evaluated, and for the results to be leveraged in the development of process-based models of time-dependent soil cation exchange

5. Conclusions

Soil biogeochemical modeling suggests that cation exchange dynamics in agricultural soils can lead to significant lags between alkalinity input from EW feedstocks and climate-relevant CDR. Lag times can vary locally from less than a year to many decades and will be controlled by background soil characteristics, land management practice, and land use history. In some cases, carbon removal lags can be reduced through thoughtful site selection and/or optimized soil pH management. However, carbon removal lags induced by soil cation storage should be ubiquitous in the field, and EW deployments that commodify carbon removal through charge balance must take storage-induced removal lags into account. In the near-term, this will require rigorous and transparent validation of reaction-transport models against real-world observations of alkalinity throughput in managed lands.

Data Availability Statement:

Observational datasets used for model spin-up and tuning are: temperature [54], soil moisture [55], runoff/infiltration [34], soil pH [53], soil organic matter [53], cation exchange capacity [56], soil nitrification rate [57], base saturation [62], soil erosion rate [58], soil porosity [59], cropland fraction [60], net primary production [61]. The model code used here (SCEPTER-v1.0) is publicly available in [32].

Funding: CTR, NJP, and SZ acknowledge support from the U.S. Department of Energy, Office of Science Energy Earthshot Initiative. CTR and NJP acknowledge funding from the U.S. Department of Agriculture and the Grantham Foundation. NJP and TJS acknowledge funding from the Yale Center for Natural Carbon Capture (YCNCC). TJS acknowledges funding from the Swiss National Science Foundation (SNSF; P500PN_210790).

Author contributions:

Conceptualization: YK, CTR, NJP
Methodology: YK, SZ, CTR, NJP
Investigation: YK, SZ, CTR, NJP
Visualization: YK, CTR, NJP
Funding acquisition: CTR, NJP
Project administration: CTR, NJP
Supervision: CTR, NJP
Writing – original draft: CTR, YK
Writing – review & editing: YK, CTR, NJP, SZ, JJ, TJS

Competing interests: JJ is employed by Mati Carbon, A B-Corp owned by the not-for-profit organization Swaniti Initiative.

References:

1. IPCC, *Global Warming of 1.5ºC. An IPCC Special Report on the impacts of global warming of 1.5ºC above pre-industrial levels and related global greenhouse gas emission pathways, in the context of strengthening the global response to the threat of climate change, sustainable development, and efforts to eradicate poverty*, V. Masson-Delmonte, et al., Editors. 2018, Cambridge University Press: Cambridge, UK and New York, NY, USA, doi:10.1017/9781009157940.

2. Rogelj, J., et al., *Scenarios toward limiting global mean temperature increase below 1.5ºC.* Nature Climate Change, 2018. **8**: p. 325-332.

3. Smith, S.M., et al., *The State of Carbon Dioxide Removal - 2nd Edition*. 2024.

4. Beerling, D.J., et al., *Enhanced weathering in the US Corn Belt delivers carbon removal with agronomic benefits.* Proceedings of the National Academy of Sciences, USA, 2024. **121**.

5. Beerling, D.J., et al., *Potential for large-scale CO2 removal via enhanced rock weathering with croplands.* Nature, 2020. **583**: p. 242-248.

6. Kantzas, E.P., et al., *Substantial carbon drawdown potential from enhanced rock weathering in the United Kingdom.* Nature Geoscience, 2022. **15**: p. 382-389.

7. Taylor, L.L., et al., *Enhanced weathering strategies for stabilizing climate and averting ocean acidification.* Nature Climate Change, 2016. **6**: p. 402-406.

8. Zhang, S., et al., *River chemistry constraints on the carbon capture potential of surficial enhanced rock weathering.* Limnology and Oceanography, 2022.

9. Kanzaki, Y., N.J. Planavsky, and C.T. Reinhard, *New estimates of the storage permanence and ocean co-benefits of enhanced rock weathering.* PNAS Nexus, 2023. **2**.

10. Baek, S.H., et al., *Impact of climate on the global capacity for enhanced rock weathering on croplands.* Earth's Future, 2023. **11**.

11. Renforth, P. and G. Henderson, *Assessing ocean alkalinity for carbon sequestration.* Reviews of Geophysics, 2017. **55**: p. 636-674.

12. Lord, N.S., et al., *An impulse response function for the "long tail" of excess atmospheric CO2 in an Earth system model.* Global Biogeochemical Cycles, 2015. **30**: p. 2-17.

13. Oh, N.-H. and P.A. Raymond, *Contribution of agricultural liming to riverine bicarbonate export and CO2 sequestration in the Ohio River basin.* Global Biogeochemical Cycles, 2006. **20**.

14. Hamilton, S.K., et al., *Evidence for carbon sequestration by agricultural liming.* Global Biogeochemical Cycles, 2007. **21**.

15. Beerling, D.J., et al., *Farming with crops and rocks to address global climate, food and soil security.* Nature Plants, 2018. **4**: p. 138-147.

16. Calabrese, S., et al., *Nano- to global-scale uncertainties in terrestrial enhanced weathering.* Environmental Science & Technology, 2022.

17. Lal, R., *Carbon management in agricultural soils.* Mitigation and Adaptation Strategies for Global Change, 2007. **12**: p. 303-322.

18. Bluth, G.J.S. and L.R. Kump, *Lithologic and climatologic controls of river chemistry.* Geochimica et Cosmochimica Acta, 1994. **58**: p. 2341-2359.

19. Knapp, W.J. and E.T. Tipper, *The efficacy of enhanced carbonate weathering for carbon dioxide sequestration.* Frontiers in Climate, 2022. **4**.

20. Harrington, K.J., R.G. Hilton, and G. Henderson, *Implications of the riverine response to enhanced weathering for CO2 removal in the UK.* Applied Geochemistry, 2023. **152**.

21. Spencer, W.F., *Influence of cation-exchange reactions on retention and availability of cations in sandy soils.* Soil Science, 1954. **77**: p. 129-136.

22. Bolt, G.H., M.G.M. Bruggenwert, and A. Kamphorst, *Adsorption of cations by soil*, in *Developments in Soil Science*, G.H. Bolt and M.G.M. Bruggenwert, Editors. 1976. p. 54-90.

23. Appelo, C.A.J., *Cation and proton exchange, pH variations, and carbonate reactions in a freshening aquifer.* Water Resources Research, 1994. **30**: p. 2793-2805.

24. Reershemius, T., et al., *Initial validation of a soil-based mass-balance approach for empirical monitoring of enhanced rock weathering rates.* Environmental Science & Technology, 2023. **57**: p. 19497-19507.

25. Suhrhoff, T.J., et al., *A tool for assessing the sensitivity of soil-based approaches for quantifying enhanced weathering: a US case study.* Frontiers in Climate, 2024. **6**.

26. Clarkson, M.O., et al., *A review of measurement for quantification of carbon dioxide removal by enhanced weathering in soil.* Frontiers in Climate, 2024. **6**.

27. Holden, F.J., et al., *In-field carbon dioxide removal via weathering of crushed basalt applied to acidic tropical agricultural soil.* Science of the Total Environment, 2024. **955**.

28. Fearnside, P.M., D.A. Lashof, and P. Moura-Costa, *Accounting for time in mitigating global warming through land-use change and forestry.* Mitigation and Adaptation Strategies for Global Change, 2000. **5**: p. 239-270.

29. Richards, K.R., *The time value of carbon in bottom-up studies.* Critical Reviews in Environmental Science and Technology, 1997. **27**: p. S279-S292.

30. Groom, B. and F. Venmas, *The social value of offsets.* Nature, 2023. **619**: p. 768-773.

31. van Kooten, G.C., P. Withey, and C.M.T. Johnston, *Climate urgency and the timing of carbon fluxes.* Biomass and Bioenergy, 2021. **151**.

32. Kanzaki, Y., et al., *In-silico calculation of soil pH by SCEPTER v1.0.* Geoscientific Model Development, 2024. **17**: p. 4515-4532.

33. Kanzaki, Y., et al., *Soil Cycles of Elements simulator for Predicting TERrestrial regulation of greenhouse gases: SCEPTER v0.9.* Geoscientific Model Development, 2022. **15**: p. 4959-4990.

34. Reitz, M., et al., *Annual estimates of recharge, quick-flow runoff, and evapotranspiration for the contiguous US using empirical regression equations.* Journal of the American Water Resources Association, 2017. **53**: p. 961-983.

35. Gwiazda, R.H. and W.S. Broecker, *The separate and combined effects of temperature, soil pCO2, and organic acidity on silicate weathering in the soil environment: Formulation of a model and results.* Global Biogeochemical Cycles, 1994. **8**: p. 141-155.

36. Goddéris, Y., et al., *Time evolution of the mineralogical composition of Mississippi Valley loess over the last 10 kyr: Climate and geochemical modeling.* Geochimica et Cosmochimica Acta, 2010. **74**: p. 6357-6374.

37. Gaillardet, J., et al., *Global climate control on carbonate weathering intensity.* Chemical Geology, 2019. **527**.

38. Zeng, S., G. Kaufmann, and Z. Liu, *Natural and anthropogenic driving forces of carbonate weathering and the related carbon sink flux: a model comparison study at global scale.* Global Biogeochemical Cycles, 2022. **36**.

39. Kantola, I.B., et al., *Improved net carbon budgets in the US Midwest through direct measured impacts of enhanced weathering.* Global Change Biology, 2023. **29**: p. 7012-7028.

40. Reershemius, T. and T.J. Suhrhoff, *On error, uncertainty, and assumptions in calculating carbon dioxide removal rates by enhanced rock weathering in Kantola et al., 2023.* Global Change Biology, 2023. **30**.

41. Baldocchi, D.D., *Assessing the eddy covariance technique for evaluating carbon dioxide exchange rates of ecosystems: past, present and future.* Global Change Biology, 2003. **9**: p. 479-492.

42. Pumpanen, J., et al., *Comparison of different chamber techniques for measuring soil CO2 flux.* Agricultural and Forest Meteorology, 2004. **123**: p. 159-176.

43. Yasuda, Y., et al., *Development of a CO2 gas analyzer for monitoring soil CO2 concentrations.* Journal of Forest Research, 2007. **13**: p. 320-325.

44. Weihermüller, L., et al., *In situ soil water extraction: A review.* Journal of Environmental Quality, 2007. **36**: p. 1735-1748.

45. Larkin, C.S., et al., *Quantification of CO2 removal in a large-scale enhanced weathering field trial on an oil palm plantation in Sabah, Malaysia.* Frontiers in Climate, 2022. **4**.

46. Service, U.N.R.C., *National Agronomy Manual*. 2011, United States Department of Agriculture.

47. Balmford, A., et al., *Realizing the social value of impermanent carbon credits.* Nature Climate Change, 2023. **13**: p. 1172-1178.

48. Qiu, Y., et al., *Intermediate soil acidification induces highest nitrous oxide emissions.* Nature Communications, 2024. **15**.

49. Hénault, C., et al., *Management of soil pH promotes nitrous oxide reduction and thus mitigates soil emissions of this greenhouse gas.* Nature Scientific Reports, 2019. **9**.

50. Cui, X., et al., *The global potential for mitigating nitrous oxide emissions from croplands.* One Earth, 2024. **7**(3): p. 401-420.

51. Grados, D., et al., *Synthesizing the evidence of nitrous oxide mitigation practices in agroecosystems.* Environmental Research Letters, 2022. **17**(11): p. 114024.

52. Lu, C., et al., *Century-long changes and drivers of soil nitrous oxide (N2O) emissions across the contiguous United States.* Global Change Biology, 2021. **28**: p. 2505-2524.

53. Poggio, L., et al., *SoilGrids 2.0: Producing soil information for the globe with quantified spatial uncertainty.* Soil, 2021. **7**: p. 217-240.

54. Fick, S.E. and R.J. Hijmans, *WorldClim 2: new 1km spatial resolution climate surfaces for global land areas* International Journal of Climatology, 2017. **37**: p. 4302-4315.

55. Wang, Y., et al., *Development of observation-based global multilayer soil moisture products for 1970 to 2016.* Earth System Science Data, 2021. **13**: p. 4385-4405.

56. Liu, S., et al., *NACP MsTMIP: Unified North American Soil Map. ORNL DAAC, Oak Ridge, Tennessee, USA.* 2014; Available from: https://doi.org/10.3334/ORNLDAAC/1242.

57. Pan, B., et al., *New approach for predicting nitrification and its fraction of N2O emissions in global terrestrial ecosystems.* Environmental Research Letters, 2021. **16**.

58. USDA, *RCA Appraisal 2011*. 2011: Washington, DC.

59. Rodell, M., et al., *The Global Land Data Assimilation System.* Bulletin of the American Meteorological Society, 2004. **85**: p. 381-394.

60. Tuanmu, M.N. and W. Jetz, *A global 1-km consensus land-cover product for biodiversity and ecosystem modeling.* Global Ecology and Biogeography, 2014. **23**: p. 1031-1045.

61. Zhao, M., et al., *Improvements of the MODIS terrestrial gross and net primary production global data set.* Remote Sensing of Environment, 2005. **95**: p. 164-176.

62. Batjes, N.H., *Harmonised soil property values for broad-scale modelling (WISE30sec) with estimates of global soil carbon stocks.* Geoderma, 2016. **269**: p. 61-68.

TABLES

Table 1. Sources of observational data for model spin-up and tuning.

Parameter	Observational Dataset
Temperature	[54]
Soil moisture	[55]
Runoff/infiltration	[34]
Soil pH	[53]
Soil organic matter	[53]
Cation exchange capacity	[56]
Nitrification rate	[57]
Base saturation	[62]
Soil erosion	[58]
Soil porosity	[59]
Cropland fraction	[60]
Net primary production (NPP)	[61]

FIGURES:

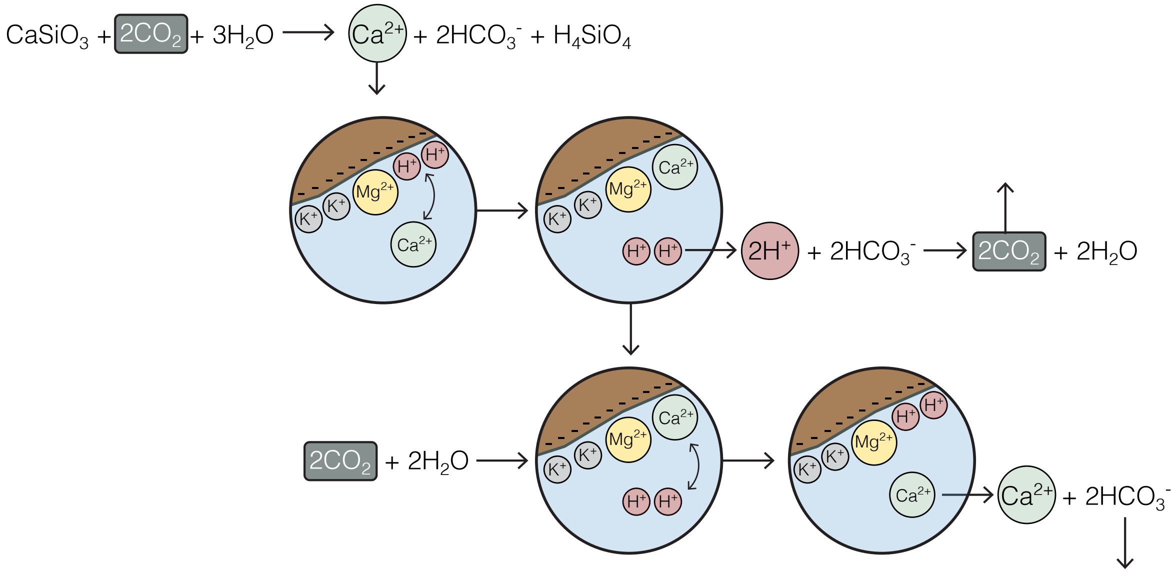

Figure 1. Schematic depiction of cation exchange dynamics that can lead to lag in carbon dioxide removal (CDR) following alkaline feedstock dissolution. In this case, wollastonite ($CaSiO_3$) is dissolved by carbonic acid in the soil, releasing calcium (Ca^{2+}) that is charge balanced by the production of bicarbonate (HCO_3^-). Exchange of dissolved Ca^{2+} onto the soil exchange complex then displaces an equivalent charge of protons (H^+). These protons then react with HCO_3^-, driving CO_2 production and undoing the initial CDR. It is only when the Ca^{2+} released from feedstock dissolution is exchanged back into solution that CDR will occur.

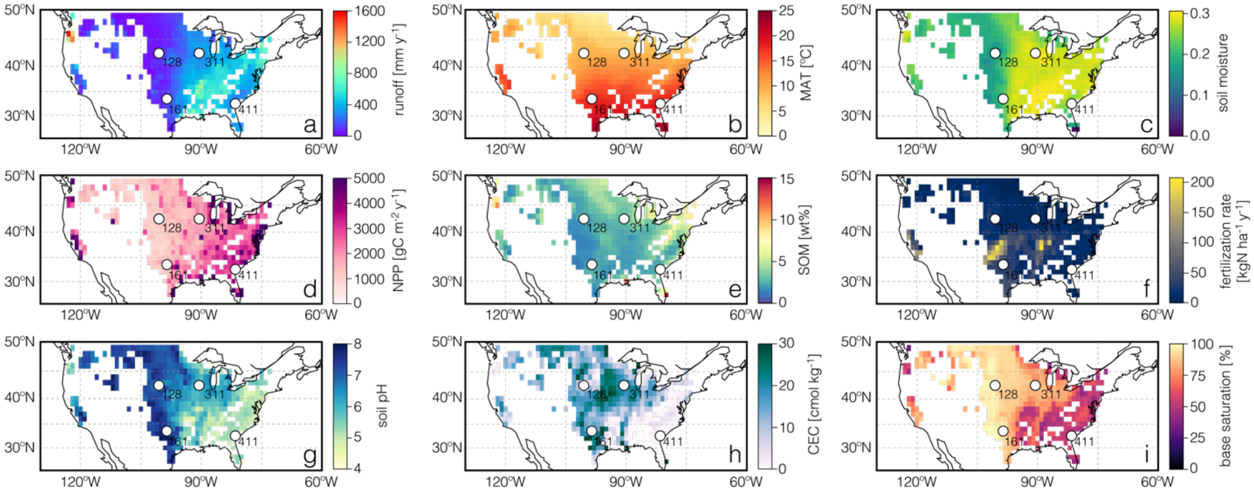

Figure 2. Gridded input data and boundary conditions from the coterminous U.S. used in our reaction-transport model. Key input parameters include runoff (a), mean annual air temperature (MAT; b), soil moisture (c), above ground net primary production (NPP; d), soil organic matter (SOM; e), fertilization rate (f), initial soil pH (g), soil cation exchange capacity (CEC; h), and soil base saturation (i). Also shown are the four site locations discussed in the text (open circles), labelled by site number.

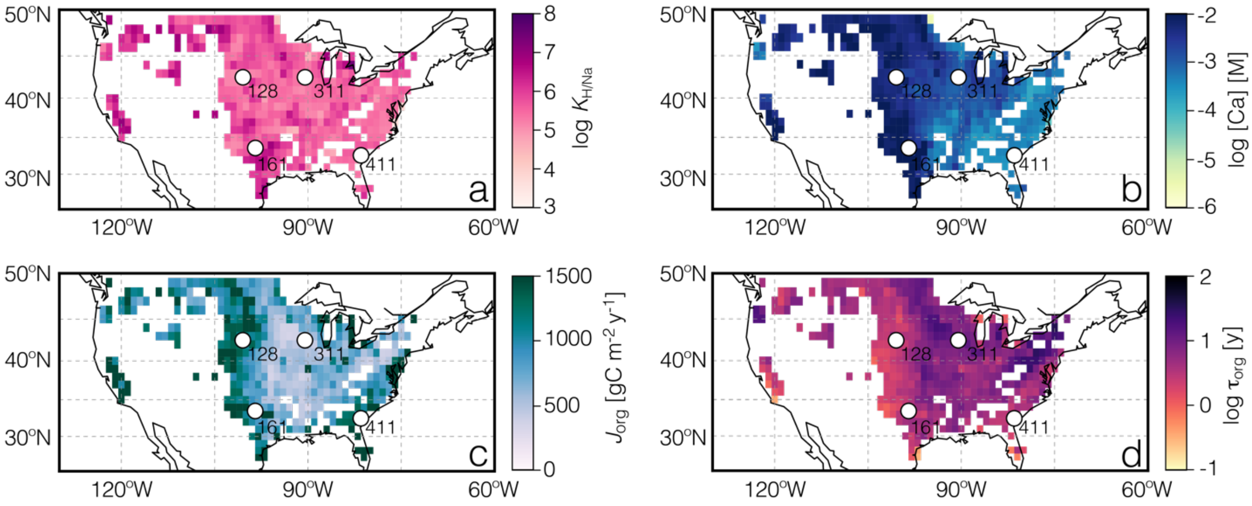

Figure 3. Results for gridded tuned parameters obtained during model spinup. Shown are soil cation exchange coefficients ($K_{H/Na}$; a), soil surface dissolved calcium concentrations ([Ca]; b), organic carbon fluxes to the soil surface (J_{org}; c), and turnover times for soil organic carbon (τ_{org}; d). Also shown are the four site locations discussed in the text (open circles), labelled by site number. See Supporting Information for validation of individual tuned model parameters.

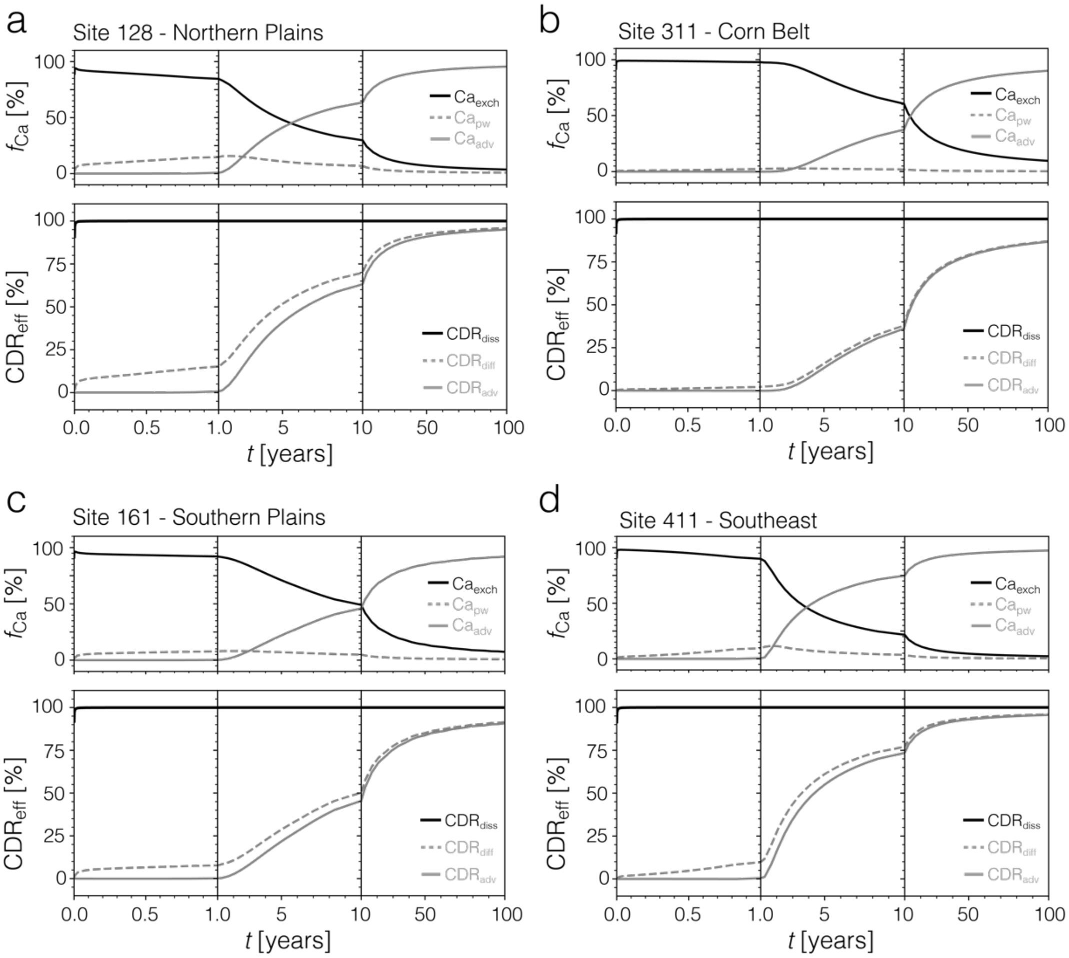

Figure 4. Time-dependent cation and CO_2 removal dynamics for the four sites discussed in the text. The upper panel for each site shows the relative distribution of calcium (Ca), the primary cation tracer in our simulations, between dissolved porewater Ca (Ca_{pw}), exchangeable Ca (Ca_{exch}), and Ca advecting through the soil column (Ca_{adv}). Values are column-integrated across the 0.5-m model domain, and are normalized relative to corresponding control simulations. The lower panel for each site shows the carbon dioxide removal efficiency relative to perfect (stoichiometric) removal (CDR_{eff}) according to three CDR metrics — tracking dissolution of the solid phase (CDR_{diss}), tracking changes in soil CO_2 diffusion (CDR_{diff}), and tracking advection of dissolved inorganic carbon (DIC) out of the model domain (CDR_{adv}). Note the non-linear *x*-axis scaling.

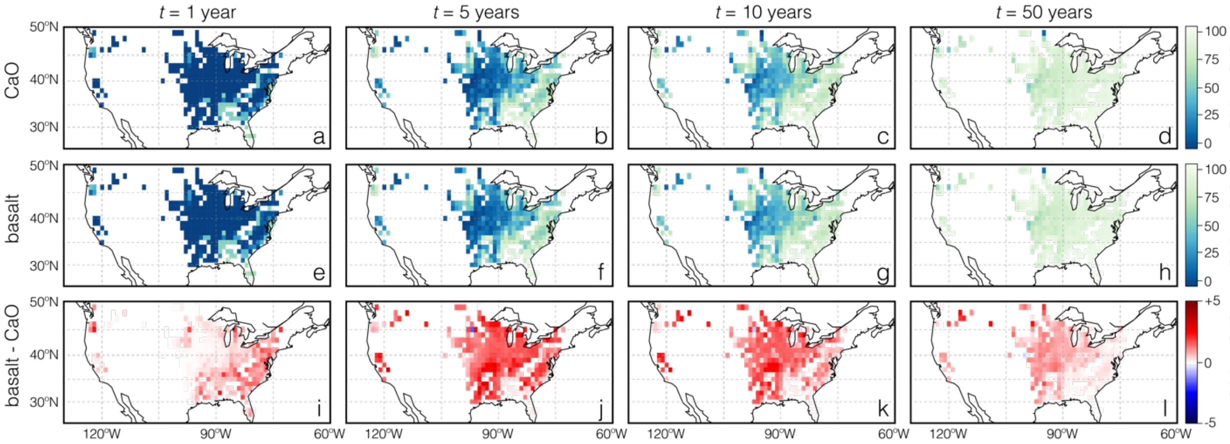

Figure 5. Regional variability in carbon dioxide removal efficiency relative to stoichiometric removal (CDR_{eff}) over time for the default (CaO) and "instantaneous" basalt cases (see text). Shown from left to right are cumulative CDR_{eff} values for time horizons of 1, 5, 10, and 50 years from the start of feedstock application. (a-d) CDR_{eff} values relative to changes in the advection of dissolved inorganic carbon (DIC) out of the model domain (CDR_{adv}) for the default case with CaO as a feedstock; (e-h) CDR_{eff} values relative to changes in the advection of dissolved inorganic carbon (DIC) out of the model domain (CDR_{adv}) using instantaneously dissolving basalt as a feedstock. (i-l) difference between CaO and instantaneous basalt cases in the advection of dissolved inorganic carbon (DIC) out of the model domain (ΔCDR_{adv}).

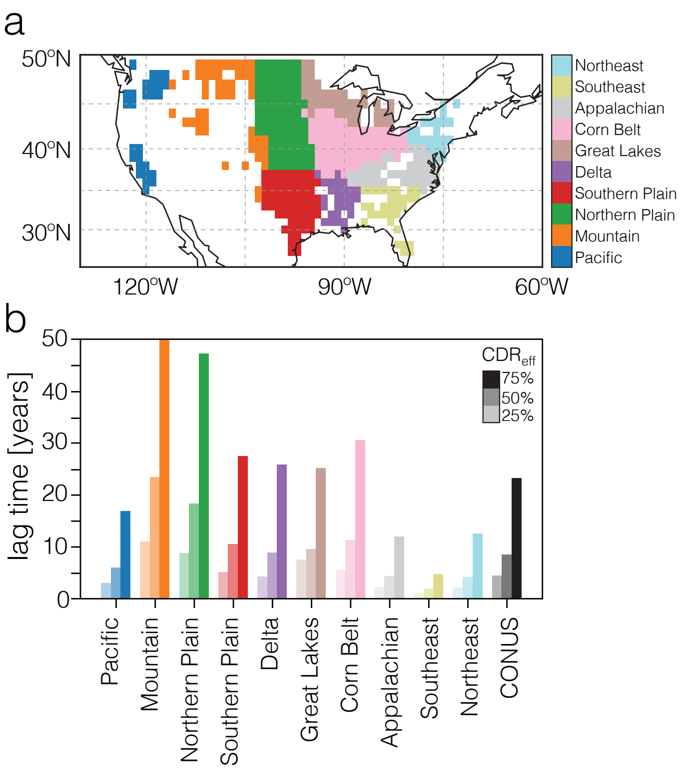

Figure 6. Aggregated regional lag times to achieve 25, 50, and 75% CO_2 removal efficiency (CDR_{eff}) relative to changes in CO_2 diffusion for the CaO deployment scenario. Regional lag times (bottom) are calculated as the average of lag times at all sites within each region (top) weighted by CaO deployment fluxes at each individual site.

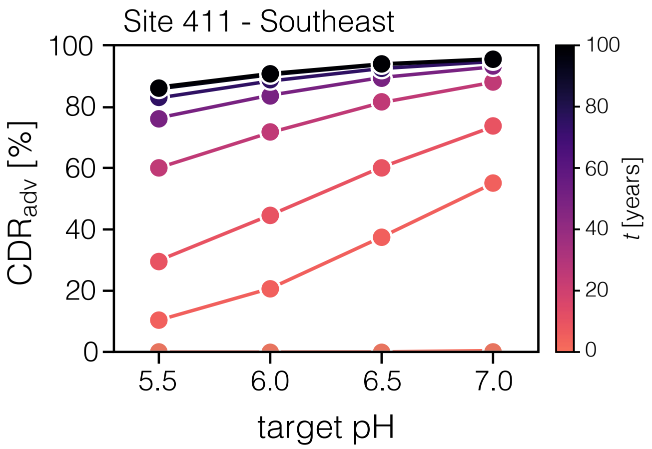

Figure 7. Example simulations from Site 411 (Southeast region) showing the impact of target soil pH on advective CDR efficiency (CDR$_{adv}$). Results are shown for various time horizons (*t*) after initial alkalinity modification. Increasing steady-state soil pH results in more rapid shift in base saturation of the soil exchange complex, reducing the timescale required to achieve a given CDR efficiency. This effect is particularly strong on sub-decadal timescales.

Environmental Research Letters

Supporting Information for

Soil cation storage is a key control on the carbon removal dynamics of enhanced weathering

Y. Kanzaki[1], N.J. Planavsky[2,3], S. Zhang[4], J. Jordan[5], [2,3]T.J. Suhrhoff, C.T. Reinhard[1*]

[1]School of Earth and Atmospheric Sciences, Georgia Institute of Technology, Atlanta, GA, USA.

[2]Department of Earth and Planetary Sciences, Yale University, New Haven, CT, USA.

[3]Yale Center for Natural Carbon Capture, New Haven, CT, USA.

[4]Department of Oceanography, Texas A&M University, College Station, TX, USA.

[5]Porecast Research, LLC, Lawrence, KS, USA.

Contents of this file

Text S1 to S5
Figures S1 to S3
Tables S1 to S2

Introduction

This supporting information provides text and figures that support and supplement the conclusions of the main article. This includes descriptive text documenting the model spinup and tuning procedure, supplementary tables documenting data sources for validation of tuned parameters, supplementary figures showing data-model comparison, and associated references.

Text S1 – Model spinup and tuning

We initialize the model by tuning four key unknown parameters: (1) a reference soil cation exchange coefficient ($K_{\mathrm{H\backslash Na}}$; Main Text Fig. 3a); (2) a dissolved Ca^{2+} concentration at the upper boundary (e.g., specifying a background/historical alkalinity flux associated with carbonate weathering and agricultural liming; Main Text Fig. 3b); (3) input of soil organic carbon (J_{org}; Main Text Fig. 3c); and (4) SOC turnover time (τ_{org}; Main Text Fig. 3d). These values are tuned to reproduce four site-specific observational parameters while the model is forced by the other boundary conditions shown in Main Text Fig. 2: (1) soil pH (Main Text Fig. 2g); (2) soil base saturation (Main Text Fig. 2i); (3) soil organic carbon (SOC) content (Main Text Fig. 2e); and (4) soil pCO_2, which is estimated from soil temperature (Main Text Fig. 2b) and net primary productivity (NPP; Main Text Fig. 2d) according to [1]. It is important to note that the model does not currently include a process-based representation of SOC and mineral interactions, so we cannot draw conclusions regarding the impact of cations on the temporary or long-term storage of SOC in soils. In order to evaluate our parameterization of Ca storage and transport through the soil column we compare our simulations to field observations of (1) cation exchange coefficients (Text S2, Fig. S1a); and (2) Ca retardation factors – a metric for the transport times of Ca through a system relative to the fluid transport timescale (Text S3, Fig. S1b). To evaluate the tuned boundary Ca concentrations, we used gridded soil inorganic carbon (SIC) data to estimate site-specific background carbonate weathering, then compare the residual boundary Ca flux with available constraints on agricultural liming in the U.S. (Text S4, Fig. S2). Finally, we compare our tuned soil organic carbon turnover times with observed values for CONUS and with those from the land models of the Coupled Model Intercomparison Project Phase 6 (CMIP6; Text S5, Fig. S3).

Text S2 – Soil cation exchange coefficients

The formulation of cation exchange in SCEPTER is described in detail in [2]. Briefly, SCEPTER includes cation exchange with solid surfaces for H^+, Na^+, K^+, Ca^{2+}, Mg^{2+}, and Al^{3+}, with all cation exchange reactions assumed to be at equilibrium. In the model, the thermodynamic constants for cation exchange for K^+, Ca^{2+}, Mg^{2+}, and Al^{3+} are scaled to the (tuned) exchange coefficient for H-Na exchange ($K_{\mathrm{H\backslash Na}}$), according to $\log K_{Y/\mathrm{Na}} = 1.1, 0.507, 0.665$, and 0.41 for $Y =$ K, Mg, Ca, and Al, respectively [3, 4]. In order to facilitate comparison of our tuned $K_{\mathrm{H/Na}}$ values with observations, we define an apparent thermodynamic constant for H-Na exchange as:

$$K'_{\mathrm{H\backslash Na}} = \frac{f(\text{H-X})[\text{Na}^+]}{f(\text{Na-X})[\text{H}^+]} \quad , \text{(S1)}$$

where f(H-X) and f(Na-X) are the charge-fractions of H^+ and Na^+ occupying exchangeable sites, respectively, and $[H^+]$ and $[Na^+]$ are the corresponding porewater concentrations of each cation (mol L^{-1}). We compiled a database of studies reporting Na^+ and H^+ both in porewater and the exchangeable phase (Table S1) and use these data to calculate $K'_{\mathrm{H\backslash Na}}$ values according to Eq. S1. We then obtain the $K'_{\mathrm{H\backslash Na}}$ values from our initialized model ensemble according to Eq. S1, using the intrinsic $K_{\mathrm{H\backslash Na}}$ values and a factor that accounts for the surface charge effect [2, 3]. As shown in Eq. S1, the values of $K'_{\mathrm{H\backslash Na}}$ are expected to be significantly influenced by porewater pH and therefore we compare values in $\log K'_{\mathrm{H\backslash Na}}$-pH space (Fig. S1a). Observed $K'_{\mathrm{H\backslash Na}}$ values show considerable variability and in many cases are characterized by ranging over orders of magnitude. However, both the general $\log K'_{\mathrm{H\backslash Na}}$-pH scaling and absolute values for exchange coefficients are consistent between the observation and our simulation at a comparable porewater pH range (Fig. S1a).

Text S3 – Retardation factor for soil Ca

One can obtain a Ca retardation factor (R_{Ca}) – the relative partitioning of Ca or any solute in the mobile phase moving through a mixed-phase system – in one of two ways: (1) by conducting "breakthrough" experiments in which Ca transport is examined relative to the transport of the fluid; or (2) direct calculation of R_{Ca} if the Ca distribution between porewater and the soil exchangeable phase is known. The first approach is challenging when attempting to compare model simulations with field data, in large part because breakthrough conditions in the field are difficult to control and because breakthrough dynamics can change with e.g., the initially loaded cation in the system [3]. However, Ca distributions are often readily available in the literature, allowing us to estimate R_{Ca} values based on the second approach. We calculate retardation factor for Ca according to:

$$R_{\mathrm{Ca}} = 1 + \frac{<\mathrm{Ca\text{-}X}>}{\theta C_{\mathrm{Ca}}} \quad , \text{(S2)}$$

where <Ca-X> and C_{Ca} represent the concentrations of exchangeable Ca (mol $\mathrm{m^{-3}}$ soil) and aqueous Ca (mol $\mathrm{m^{-3}}$ porewater), respectively and θ denotes soil moisture ($\mathrm{m^3}$ porewater $\mathrm{m^{-3}}$ soil). We compiled a database of studies that report both <Ca-X> and C_{Ca} (Table S2) and use these to calculate R_{Ca} based on Eq. S2. We assume a range for θ consistent with the observational data product used in the geospatial ensemble (0.13 to 0.31; Main Text Fig. 2). We then obtain R_{Ca} values from our initialized model ensemble from all sites, using the observed θ value for each site. It is clear from Eq. S2 that CEC is a dominant control over R_{Ca} [e.g., 5], so we compare results from the initialized model ensemble to observations in CEC-R_{Ca} space (Fig. S1b). As with $K'_{\mathrm{H\backslash Na}}$ values, estimates of R_{Ca} show considerable variability across the observed CEC range and can range considerably at a given CEC value. Nevertheless, our simulated values for R_{Ca} are within observed variability across a range of systems, indicating that our model does not artificially reduce the effectiveness of Ca transport.

Text S4 – Historical agricultural liming

Our initialization procedure includes a tuned calcium concentration at the upper boundary (Main Text Fig. 3b), which essentially represents a boundary alkalinity flux required to achieve observed soil pH (Main Text Fig. 2g). This boundary condition can be readily replaced with a $\mathrm{CaCO_3}$ input flux, which represents a net soil $\mathrm{CaCO_3}$ dissolution flux coming from both inputs due to agricultural liming and natural background $\mathrm{CaCO_3}$ weathering. In order to roughly estimate the background natural $\mathrm{CaCO_3}$ weathering flux we obtain soil $\mathrm{CaCO_3}$ (wt%) data at different soil depths from the Global Soil Dataset for use in Earth System Models [GSDE; 6], with available depths of 4.5, 9.1, 16.1, 28.9, 49.3, 82.9, 138.3, and 229.6 cm (Fig. S2a-c). These data are used to estimate a background $\mathrm{CaCO_3}$ weathering rate according to:

$$J_{weath} = w\rho\Delta\mathrm{CaCO_3} \quad , \text{(S3)}$$

where w is the cropland erosion rate [7], ρ is the bulk soil density (assumed here to be 1.5×10^6 $\mathrm{g/m^3}$), and $\Delta\mathrm{CaCO_3}$ is the difference in $\mathrm{CaCO_3}$ content between the deepest depth for cropland soils (assumed here to be either 49.3 or 82.9 cm) and the topmost soil layer (4.5 cm). Using this approach (Fig. S2d-f), we estimate a background $\mathrm{CaCO_3}$ weathering flux between 16 and 40 megatons (Mt = 10^6 tons) of $CaCO_3$ per year for our cropland model ensemble using lower soil depths of 49.3 and 82.9 cm, respectively. This can be compared with an estimate for total $CaCO_3$ weathering from major CONUS rivers of ~80 Mt$CaCO_3$ y^{-1} [8], which is of the same order but larger because it also includes all non-cropland areas. If we subtract this background weathering from the gross $CaCO_3$ input flux we estimate during initialization (Fig. S2g-i), we find a median area-normalized flux for croplands (18-25 g$CaCO_3$ m^{-2} y^{-1}), consistent with estimates of agricultural liming in the Mississippi River basin [9]. When integrated across CONUS croplands we obtain an estimate of 18-31 Mt$CaCO_3$ y^{-1}, which can be compared to an estimated agricultural liming flux of ~20-40 Mt$CaCO_3$ y^{-1} from [10]. Though there remains a pressing need for robust gridded datasets of agricultural liming in cropland systems in the U.S. and globally, our results suggest that the upper boundary we place on alkalinity input during initialization is fully in line with our understanding of background and anthropogenic alkalinity fluxes to cropland soils in the U.S.

Text S5 – Soil respiration and SOC turnover

By default, SCEPTER employs a simplified representation of soil organic carbon (SOC) cycling, with three SOC classes of differing reactivity and a Michaelis-Menten dependence on soil oxygen [see 11]. In the analysis presented here, we use observations of MAT and NPP (Main Text Fig. 2b,d) to derive an estimate of soil pCO_2 according to [1], then tune the input flux of SOC (Main Text Fig. 3c) and a turnover time representing organic matter reactivity (Main Text Fig. 3d) to match soil pCO_2 and SOC content (Main Text Fig. 2e). Our tuned values of SOC turnover time (τ_{org}, in years) can be compared with observations and more sophisticated (IPCC-class) land surface models by defining turnover time as SOC storage (gC m^{-2}) divided by soil respiration rate (gC m^{-2} y^{-1}), following [12]. We obtain observational SOC storage data from GSDE (Shangguan et al., 2014) and soil respiration rates from CARDAMOM [13]. Our model assumes a soil mixed layer of 25 cm, so we compare our calculated turnover times to observations for the upper 28.9 cm in GSDE (Fig. S3a,b). Our estimated τ_{org} values are generally consistent with those from GSDE/CARDAMOM, though there is a clear bias toward higher values in the Northeast U.S. and lower values in the Northern Plains region (Fig. S3b). These results can be compared to IPCC-class land surface models, using an 82.9 cm depth horizon from GSDE as CMIP6 models represent the upper 1 m of soil by default (Fig. S3c,d). We find a comparable distribution of bias from GSDE/CARDAMOM observations in the CMIP6 ensemble mean (Fig. S3d) to those of our initialized model ensemble. Fully evaluating the mechanisms for bias in model SOC turnover and storage is a significant issue in Earth system models that is well beyond the scope of this study. However, these results indicate that our tuned values for SOC turnover are well in line with existing land surface models.

Reference	Short description	Note
[3]	Dutch soil/sediment	
[2, 14]	Mesocosm at Yale greenhouse	Soil solution and soil chemistry listed in Kanzaki et al. (2024)
[15]	Chinese soil at tea plantation	
[16]	Canterbury New Zealand	C_{Ca} is from soil saturation paste extract. CEC and f(Ca-X) are read from diagram
[17]	Pasture Pine in New Zealand	For 10-20 cm solution pH is from tension lysimetry at 22 cm (other from centrifugation)
[18]	Forest soil Norway	
[19]	European soil	
[20]	Douglas fir stand in France	C_{Ca} is read from diagram
[21]	Volcanic soils in Iceland	
[22]	Maury silt loam	$\log K'_{H\backslash Na} = \log K'_{H\backslash K} + 0.6$ based on $K'_{H\backslash K}$ and assuming $\log K'_{K\backslash Na} = 0.6$
[23, 24]	Hubbard Brook Experimental Forest in New Hampshire	F(Ca-X) and f(H-X) are extrapolated when missing while soil solution data exist
[25]	Canadian podzol	CEC is calculated as a function of soil pH

Table S1. References used to calculate empirical cation exchange coefficients ($K'_{H/Na}$).

Reference	Short description	Note
[2, 14]	Mesocosm at Yale greenhouse	Soil solution and soil chemistry listed in Kanzaki et al. (2024)
[16]	Canterbury New Zealand	C_{Ca} is from soil saturation paste extract
[17]	Pasture Pine in New Zealand	
[26]	Forest soil Sweden	C_{Ca} is assumed to be equivalent as base saturation
[18]	Forest soil Norway	
[19]	European soil	
[20]	Douglas fir stand in France	C_{Ca} is read from diagram
[27]	Hubbard Brook Experimental Forest in New Hampshire	
[28]	Incubation of basalt powder with Malaysian Oxisol	
[29]	130-year-old beech/oak forest in Steigerwald Germany	
[21]	Volcanic soils in Iceland	
[30]	Haplic Podzol in mature Norway spruce forest	
[22]	Maury silt loam	
[31]	Japanese paddy fields	CEC is calculated as sum of exch. base cations
[25]	Canadian podzol	CEC is calculated as a function of soil pH

Table S2. References used to calculate empirical Ca retardation factors (R_{Ca}).

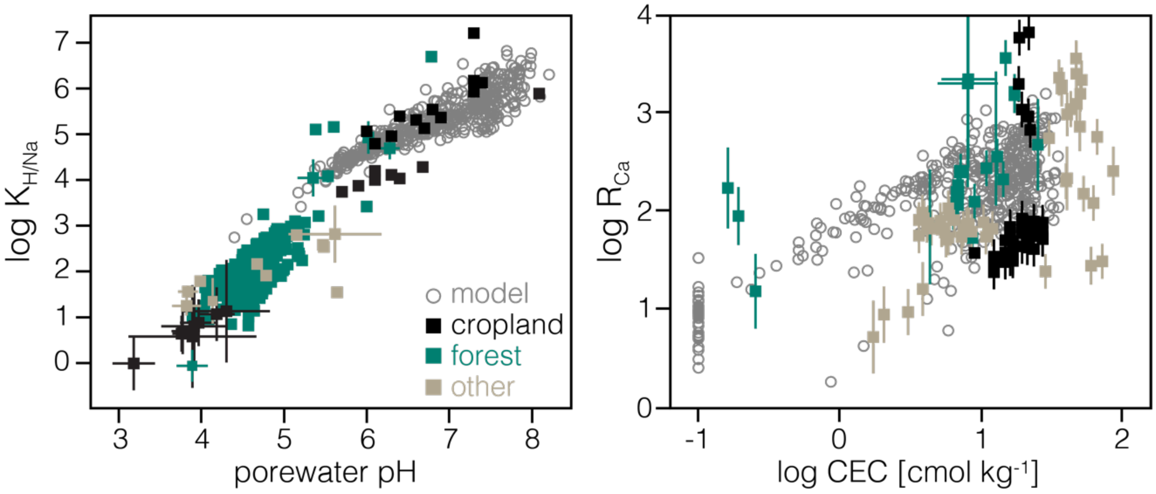

Figure S1. Comparison of log$K'_{\mathrm{H\backslash Na}}$ as a function of porewater pH (left) and logR_{Ca} as a function of log CEC (right) between the tuned model ensemble and observational data. Observed data are depicted with different colors based on the soil type from the database summarized in Tables S1 and S2.

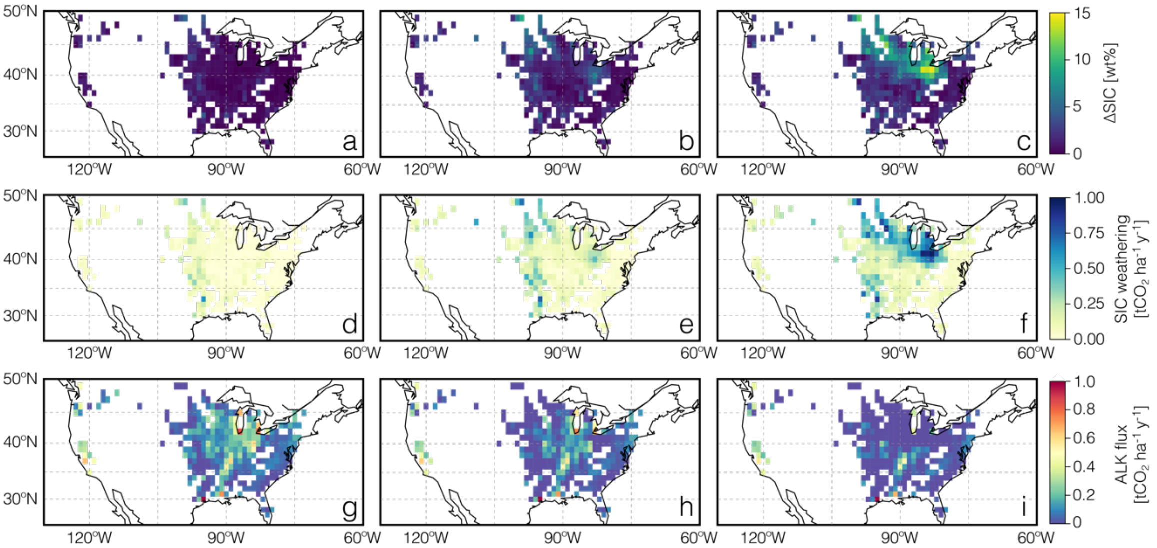

Figure S2. Estimates of soil CaCO$_3$ gradient (a-c), background CaCO$_3$ weathering flux (d-f), and inverted liming rate (g-h), across U.S. cropland. The soil CaCO$_3$ gradient is calculated based on the GSDE CaCO$_3$ dataset as the concentration difference between the bottom and surface, assuming the bottom as 49.3 (a, d, g), 82.9 (b, e, h), and 138.3 (c, f, i) cm depths, with 4.5 cm data used to represent the soil surface layer. The background CaCO$_3$ weathering flux is a function of soil CaCO$_3$ gradient, and the liming rate is calculated as the gross CaCO$_3$ input flux (equivalent to the Ca upper boundary condition; Main Text Fig. 3b) in the initialized model subtracted by background CaCO$_3$ weathering flux. See Text S4 for the details of the calculation.

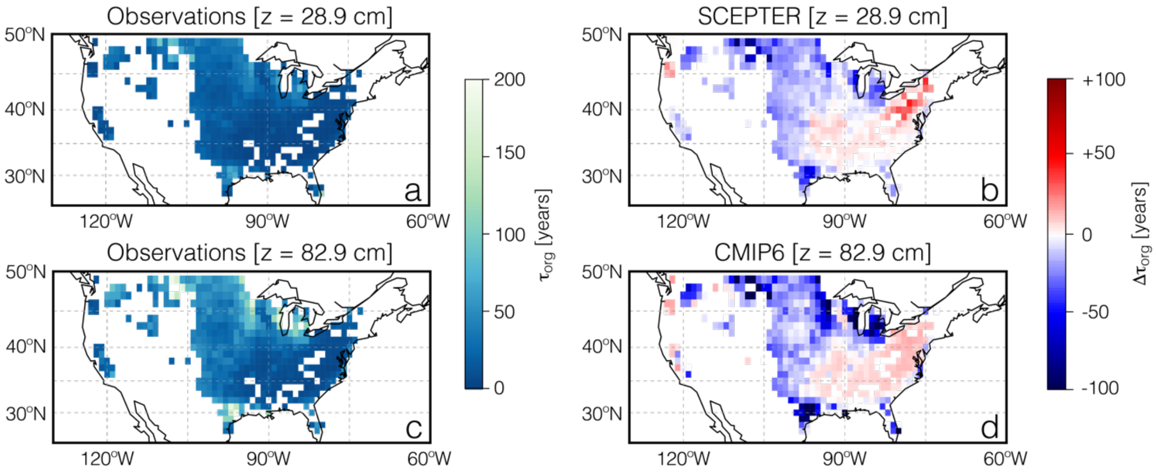

Figure S3. Comparison of turnover time for soil organic carbon (τ_{org}) between observations (a,c), SCEPTER (b), and the CMIP6 model ensemble mean (d). Observational τ_{org} values are calculated with soil respiration from CARDAMOM dataset and soil organic carbon storage from GSDE. In (a) and (c), 28.9 and 82.9 cm depths are assumed as the bottom of the organic matter storage domain in order to be comparable to the depths of simulation domains for soil organic matter in SCEPTER (25 cm) and CMIP6 models (100 cm), respectively. In (b) and (d), the differences of simulated τ_{org} values relative to the corresponding observations ($\Delta\tau_{org}$) are shown. CMIP6 results are based on the mean τ_{org} values from 22 CMIP6 Earth System models. See Text S5 for further details of the calculation.

Supporting References

1. Zeng, S., G. Kaufman, and Z. Liu, *Natural and anthropogenic driving forces of carbonate weathering and the related carbon sink flux: a model comparison study at global scale.* Global Biogeochemical Cycles, 2022. **36**.
2. Kanzaki, Y., et al., *In-silico calculation of soil pH by SCEPTER v1.0.* Geoscientific Model Development, 2024. **17**: p. 4515-4532.
3. Appelo, C.A.J., *Cation and proton exchange, pH variations, and carbonate reactions in a freshening aquifer.* Water Resources Research, 1994. **30**: p. 2793-2805.
4. Parkhurst, D.L. and C.A.J. Appelo, *User's guide to PHREEQC (Version 2) - A computer program for speciation, batch reaction, 1 dimensional transport, and inverse geochemical calculation*, in *Water-Resources Investigations Reports*. 1999, USGS.
5. Samper, J. and C. Yang, *Stochastic analysis of transport and multicomponent competitive monovalent cation exchange in aquifers.* Geosphere, 2006. **2**: p. 102-112.
6. Shangguan, W., et al., *A global soil data set for Earth system modeling.* Journal of Advances in Modeling Earth Systems, 2014. **6**: p. 249-263.
7. USDA, *RCA Appraisal 2011*. 2011: Washington, DC.
8. Gaillardet, J.D.B.L., et al., *Global silicate weathering and CO2 consumption rates deduced from the chemistry of large rivers.* Chemical Geology, 1999. **159**: p. 3-30.
9. Oh, N.-H. and P.A. Raymond, *Contribution of agricultural liming to riverine bicarbonate export and CO2 sequestration in the Ohio River basin.* Global Biogeochemical Cycles, 2006. **20**.
10. West, T.O. and A.C. McBride, *The contribution of agricultural lime to carbon dioxide emissions in the United States: dissolution, transport, and net emissions.* Agricultur, Ecosystems & Environment, 2005. **108**: p. 145-154.
11. Kanzaki, Y., et al., *Soil Cycles of Elements simulator for Predicting TERrestrial regulation of greenhouse gases: SCEPTER v0.9.* Geoscientific Model Development, 2022. **15**: p. 4959-4990.
12. Varney, R.M., et al., *Evaluation of soil carbon simulation in CMIP6 Earth system models.* Biogeosciences, 2022. **19**: p. 4671-4704.
13. Bloom, A. and M. Williams, *CARDAMOM 2001-2010 global carbon Model-Data Fusion (MDF) analysis, 2001-2010*, U.o.E.S.o. GeoSciences, Editor. 2015.
14. Chiaravalloti, I., et al., *Mitigation of soil nitrous oxide emissions during maize production with basalt amendments.* Frontiers in Climate, 2023. **5**.
15. Yang, X.D., et al., *Effects of long-term nitrogen application on soil acidification and solution chemistry of a tea plantation in China.* Agricultur, Ecosystems & Environment, 2018. **252**: p. 74-82.
16. Haynes, R.J. and K.M. Goh, *Some observations on surface soil pH, base saturation and leaching of cations under three contrasting orchard soil management practices.* Plant and Soil, 1980. **56**: p. 429-438.
17. Parfitt, R.L., et al., *Soil and solution chemistry under pasture and radiata pine in New Zealand.* Plant and Soil, 1997. **191**: p. 279-290.

18. Manderscheid, B. and E. Matzner, *Spatial and temporal variation of soil solution chemistry and ion fluxes through the soil in a mature Norway spruce (Picea abies (L.) Karst.) stand.* Biogeochemistry, 1995. **30**: p. 99-114.
19. Wang, Z., A. Göttlein, and G. Bartonek, *Effects of growing roots of Norway spruce (Picea abies [L.] Karst.) and European beech (Fagus sylvatica L.) on rhizosphere soil solution chemistry.* Journal of Plant Nutrition and Soil Science, 2001. **164**: p. 35-41.
20. Turpault, M.P., et al., *Influence of mature Douglas fir roots on the solid soil phase of the rhizosphere and its solution chemistry.* Plant and Soil, 2005. **275**: p. 327-336.
21. Opfergelt, S., et al., *Magnesium retention on the soil exchange complex controlling Mg isotope variations in soils, soil solutions and vegetation in volcanic soils, Iceland.* Geochimica et Cosmochimica Acta, 2014. **125**: p. 110-130.
22. Evangelou, V.P. and R.L. Blevins, *Soil-solution phase interactions of basic cations in long-term tillage systems.* Soil Science Society of America Journal, 1985. **49**: p. 357-362.
23. Driscoll, C.T., *Chemistry of freely-draining soil solutions at the Hubbard Brook Experimental Forest, Watershed 1, 1996-present*, E.D. Initiative, Editor. 2022.
24. Johnson, D.E., *Mass and chemistry of organic horizons and surface mineral soils on Watershed 1 at the Hubbard Brook Experimental Forest 1996-present ver 3*, E.D. Initiative, Editor. 2022.
25. Simard, R.R., L.J. Evans, and T.E. Bates, *The effects of additions of CaCO3 and P on the soil solution chemistry of a podzolic soil.* Canadian Journal of Earth Sciences, 1988. **68**: p. 41-52.
26. Giesler, R., U.S. Lundström, and H. Grip, *Comparison of soil solution chemistry assessment using zero-tension lysimeters or centrifugation.* Euopean Journal of Soil Science, 1996. **47**: p. 395-405.
27. Cho, Y., et al., *Chemical changes in soil and soil solution after calcium silicate addition to a northern hardwood forest.* Biogeochemistry, 2010. **100**: p. 3-20.
28. Anda, M., J. Shamshuddin, and C.I. Fauziah, *Improving chemical properties of a highly weathered soil using finely ground basalt rocks.* Catena, 2015. **124**: p. 147-161.
29. Chang, S.C. and E. Matzner, *The effect of beech stemflow on spatial patterns of soil solution chemistry and seepage fluxes in a mixed beech/oak stand.* Hydrological Processes, 2000. **14**: p. 135-144.
30. Hentschel, K., et al., *Effects of soil frost on nitrogen net mineralization, soil solution chemistry and seepage losses in a temprate forest.* Global Change Biology, 2009. **15**: p. 825-836.
31. Wada, S.I. and K. Odahara, *Potassium-calcium exchange in five Ap soils from paddy fields and its effect on potassium concentration in soil solution.* Soil Science and Plant Nutrition, 1993. **39**: p. 129-138.